Materials Advances

ROYAL SOCIETY OF CHEMISTRY

PAPER

View Article Online
View Journal | View Issue

Cite this: *Mater. Adv.*, 2025, **6**, 7969

Succinate coprecipitation synthesized Cr-doped Fe_2O_3 as an efficient electrocatalyst for hydrogen evolution reaction in alkaline medium

Paulin Kammi Yontchoum,[ab] Carelle Martiale Kamga Meffo,[a] Bilal Tasdemir,[c] Kenneth Mbene,[a] Cedrik Ngnintedem Yonti,[a] Bilge Saruhan,[c] Patrice Kenfack Tsobnang[d] and Roussin Lontio Fomekong *[a]

The depletion of fossil fuels and growing environmental concerns have created an urgent global demand for sustainable energy solutions. Among these, hydrogen has emerged as a pivotal energy carrier due to its high energy density and potential for clean combustion. Electrolytic water splitting, especially when powered by renewable energy, offers a promising, carbon-neutral method for hydrogen production. Yet, it is constrained by the slow kinetics of the hydrogen evolution reaction (HER) at the cathode. Thus, obtaining a performant, cheap and environmentally friendly electrocatalyst for HER becomes a big challenge. This study explores the enhancement of HER by developing Cr-doped iron oxide (Fe_2O_3) nanomaterials, synthesized *via* a co-precipitation method utilizing succinate ions. Our research demonstrates that Cr-doping significantly modifies the electronic structure and catalytic properties of iron oxide, with optical analyses revealing a bandgap reduction from 1.92 eV to 1.48 eV as Cr^{3+}-concentration increases from 2 to 6.5 atomic percent. The electrocatalytic activity for HER was notably improved, achieving an optimal overpotential of 307 mV at 10 mA cm^{-2} with a Cr-doping level of 5.5 atomic percent, which outperforms both undoped Fe_2O_3 and Cr_2O_3 alone. This performance boost is attributed to the creation of new active sites through lattice defects from chromium substitution into the iron oxide matrix. This investigation not only deepens our understanding of the structure–activity relationships in doped iron oxides but also marks a significant step toward developing efficient, economically viable electrocatalysts for sustainable hydrogen production technologies.

Received 12th June 2025,
Accepted 23rd September 2025

DOI: 10.1039/d5ma00634a

rsc.li/materials-advances

1. Introduction

The escalating global energy crisis, primarily driven by the depletion of fossil fuel reserves and the associated environmental concerns, has intensified the search for sustainable and clean energy alternatives.[1] Hydrogen, owing to its high energy density (120 MJ kg^{-1})[2] and clean combustion, has emerged as a promising energy carrier that can potentially decarbonize various sectors, including transportation and industry. Electrolytic water splitting, powered by renewable electricity, represents a particularly attractive route for hydrogen production, as it offers a carbon-neutral pathway.[3] However, the sluggish kinetics of the HER at the cathode significantly hinder the large-scale adoption of this technology.[4]

To accelerate the HER, extensive research has been devoted to the development of highly efficient electrocatalysts. Noble metals, such as platinum and iridium, exhibit exceptional catalytic activity for the HER.[5] Nevertheless, their scarcity and high cost pose significant challenges for widespread commercialization. As a result, there has been a growing interest in exploring alternative, cost-effective, and abundant materials for electrocatalysis. Transition metal oxides, particularly those based on earth-abundant elements like iron, have emerged as promising candidates due to their tunable electronic properties, high stability, and low cost.

Iron oxides, especially hematite (α-Fe_2O_3), have been extensively studied as HER and oxygen evolution reaction (OER) electrocatalysts owing to their low cost and abundance.[6–8] However, their intrinsic catalytic activity is limited by poor electrical conductivity and a large overpotential. To address these limitations, various strategies have been employed, including doping with foreign atoms to modulate the electronic

[a] *Department of Chemistry, Higher Teacher Training College, University of Yaoundé I, P.O. Box 47, Yaoundé, Cameroon. E-mail: roussin.lontio@univ-yaounde1.cm*
[b] *Institute of Condensed Matter and Nanoscience, Université catholique de Louvain 1 Place Louis Pasteur, Louvain-la-Neuve 1348, Belgium*
[c] *German Aerospace Center, Institute for Frontier Materials on Earth and in Space, Linder Hoehe, Cologne 51147, Germany*
[d] *Department of Chemistry, University of Dschang, P.O. Box 67, Dschang, Cameroon*

structure and create additional active sites.[9,10] While transition metal-doped iron oxides have been investigated for various applications such as water splitting,[11] electrolysis, battery[12] and dehydrogenation, the potential of Cr-doped Fe_2O_3 as an HER electrocatalyst remains largely unexplored. Chromium, with its variable oxidation states and potential for forming stable solid solutions with iron oxide, presents an intriguing candidate for enhancing the HER activity of this material. Previous studies have demonstrated that chromium doping can significantly alter the electronic structure and surface properties of iron oxides, leading to improved catalytic performance in various redox reactions.[13,14] Furthermore, the incorporation of chromium may introduce new active sites and modulate the adsorption/desorption kinetics of hydrogen intermediates, thereby facilitating the HER process.

In this study, we report the synthesis and characterization of chromium-doped iron oxide nanomaterials for the alkaline hydrogen evolution reaction. Since the synthesis method is known to have an impact on prepared materials, the co-precipitation method, utilizing succinate ions as a precipitating agent, was employed to synthesize these materials. The selection of the co-precipitation technique is strategic, as it offers precise control over particle size, morphology, and compositional homogeneity, all of which are critical factors influencing the electrocatalytic activity of materials. Moreover, the choice of succinate as a ligand is instrumental in modulating the properties of the resulting oxides. Succinate ions, with their bifunctional character, can coordinate with metal cations to form intermediate complexes, influencing nucleation, growth, and the final crystal structure of the precipitates.[15] This approach, compared to other synthesis methods such as sol–gel or hydrothermal, enables the creation of materials with tailored properties, enhancing their potential for the HER. By systematically varying the chromium doping level, we aim to optimize the catalytic activity of these materials for the HER.

To the best of our knowledge, this is the first report on the application of chromium-doped iron oxide synthesized by the succinic acid co-precipitation method as an electrocatalyst for the alkaline HER. This work not only contributes to the fundamental understanding of the structure–activity relationships in these materials but also provides a promising avenue for the development of cost-effective and sustainable hydrogen production technologies.

2. Experimental section

2.1. Chemicals

To produce both undoped and Cr-doped iron oxide nanomaterials, succinic acid ($C_4H_6O_4$, Sigma-Aldrich, 98.8%), lithium hydroxide monohydrate ($LiOH{\cdot}H_2O$, Sigma-Aldrich, 98.5%), ferric chloride ($FeCl_3$, Riedel de Haen, 98%), chromium(III) chloride hexahydrate ($CrCl_3{\cdot}6H_2O$, Merck, 99%), ethanol (C_2H_6O, ANALAR, 95%), and a 5% Nafion solution (Merck) were employed as the starting materials. All chemicals were used as received without further purification.

2.2. Synthesis of succinate-based Fe and Cr precursors

Iron(III) succinate (Fe-Succ) and chromium(III) succinate (Cr-Succ) were synthesized at room temperature in ethanolic solution. Succinic acid ($(CH_2)_2(COOH)_2$) was deprotonated using lithium hydroxide monohydrate ($LiOH.H_2O$), followed by the addition of either chromium(III) chloride hexahydrate ($CrCl_3{\cdot}6H_2O$) or iron(III) chloride ($FeCl_3$) dissolved in ethanol. The resulting mixtures were stirred for 90 minutes, filtered, washed, and dried at 100 °C for 30 minutes.

A series of chromium-doped iron succinate samples were synthesized *via* co-precipitation in an ethanolic medium. The chromium atomic percentage, relative to the total metal content (Cr/(Cr + Fe)), was systematically varied at 2, 4, 5.5, and 6.5 atomic percent (at%), yielding samples designated as FeCr-Suc1, FeCr-Suc2, FeCr-Suc3, and FeCr-Suc4, respectively. For instance, to prepare FeCr-Suc1, 4.92 mmol of succinic acid ($(CH_2)_2(COOH)_2$) was initially deprotonated using 9.84 mmol of $LiOH.H_2O$. Subsequently, a mixture of dissolved salts, including 3.21 mmol (0.52 g) of iron(III) chloride ($FeCl_3$) and 0.07 mmol (0.02 g) of $CrCl_3{\cdot}6H_2O$, was added drop by drop in the desired proportions. The mixture was stirred for 90 minutes, filtered, washed, and dried in an oven at 100 °C for 30 minutes, as illustrated in Fig. 1.

2.3. Synthesis of oxide materials by calcination of the Succinate-based Fe and Cr precursors

Precursor powders, each weighing one gram (1 g), were subjected to calcination in a ceramic vessel within a muffle furnace at 650 °C for 60 minutes under ambient air conditions. The heating rate was maintained at 10 °C per minute. Through this process, iron oxide (Fe_2O_3), chromium oxide (Cr_2O_3), and Cr-doped Fe_2O_3 samples ($Cr_xFe_{2-x}O_3$) were synthesized, with chromium atomic percentages relative to the total metal content (Cr/(Cr + Fe)) at 2, 4, 5.5, and 6.5 atomic percent. These samples, designated as FeCrO-1, FeCrO-2, FeCrO-3, and FeCrO-4 respectively, were derived from the pyrolysis of their corresponding precursors (FeCr-Suc1, FeCr-Suc2, FeCr-Suc3, and FeCr-Suc4) at 650 °C, as depicted in Fig. 1. The selection of succinate as a ligand is strategic due to its bifunctional carboxylate groups, which enable effective chelation with metal ions. Compared to other ligands such as citrate or oxalate, succinate offers better control over particle dispersion and crystallinity, which are crucial for electrocatalytic applications.[15]

2.4. Materials characterization

Fourier Transform Infrared (FTIR) spectra were acquired using a Nicolet 6700 FTIR spectrometer at ambient temperature. Spectra were recorded over a spectral range of 4000 to 373 cm^{-1}, with a resolution of 4 cm^{-1}, for both precursor and oxide samples.

Powder x-ray diffraction (XRD) patterns for all synthesized oxide samples were obtained using a Bruker D8 Advance diffractometer (Bruker, Germany) equipped with a Cu Kα radiation source (λ = 1.5406 Å). Data were collected in a 2θ range of 5° to 100° with a step size of 0.05°.

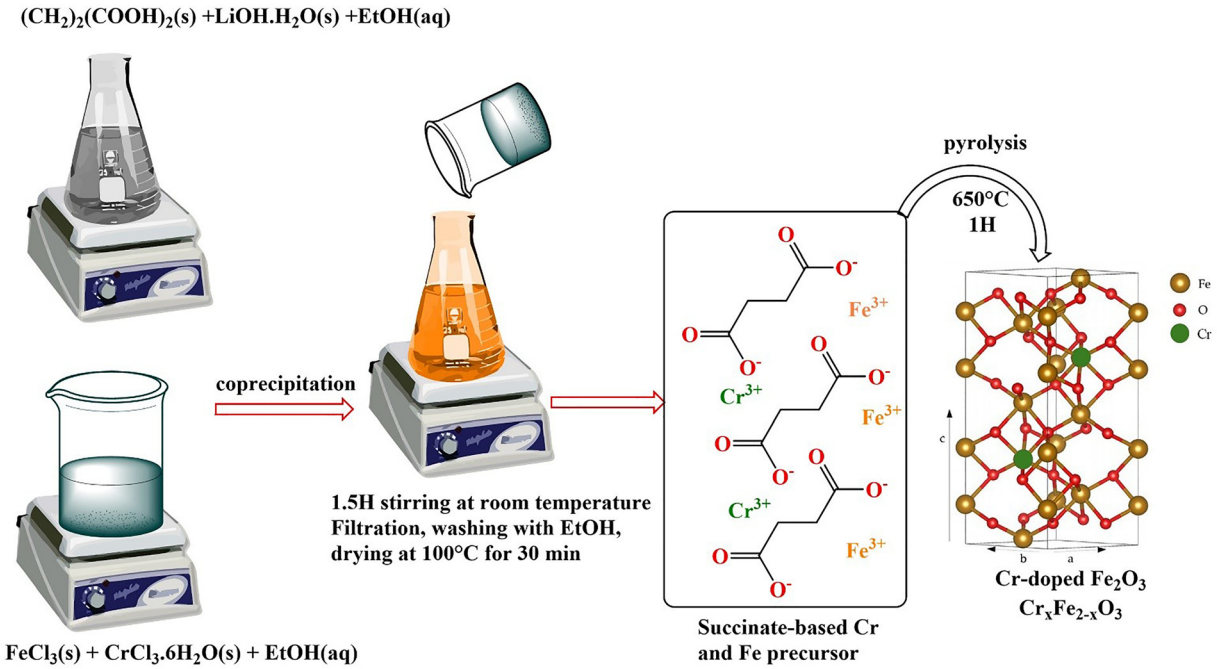

Fig. 1 Synthesis route of all the developed Cr-doped Fe_2O_3.

Morphological characterization was carried out using both scanning electron microscopy (SEM) and scanning transmission electron microscopy (STEM). SEM imaging was performed on a Zeiss Ultra 55 microscope (Zeiss, Jena, Germany) operated at an accelerating voltage of 8 kV. Prior to observation, all samples were sputter-coated with a thin platinum layer to minimize charging effects. Complementary high-resolution STEM analysis was conducted using a SM-74240RTED microscope (JEOL, Belgium) operated at an accelerating voltage of 30 kV. Elemental composition analysis was conducted using energy-dispersive X-ray spectroscopy (EDX).

The optical properties of the samples were investigated using a Jasco V750 UV-vis spectrophotometer equipped with an integrating sphere. Absorbance spectra were recorded between 200 and 800 nm in continuous scan mode at a rate of 400 nm min^{-1}.

2.5. Electrochemical properties analysis

Electrochemical HER measurements were conducted at ambient temperature using a CORRTEST CS310M instrument in a standard three-electrode configuration. An Ag/AgCl electrode served as the reference electrode and was pre-conditioned in 1 M KOH and remained stable, with potential variation under 5 mV over 24 hours. A carbon rod was employed as the counter electrode, and glassy carbon (GC) coated with the synthesized materials was used as the working electrode. The catalyst ink was prepared by dispersing 1.5 mg of Cr-doped Fe_2O_3 in 0.5 mL of 95° ethanol. The mixture was sonicated for 10 minutes to achieve homogeneous dispersion. The working electrode was prepared by drop-casting 40 μL of a catalyst ink containing 0.12 mg of active material onto a GC substrate, followed by drying and the application of a Nafion solution (5 wt%) as a binder. The electrodes were then dried at 55 °C for 15 minutes to stabilize the coating.

The measured potentials were converted to the reversible hydrogen electrode (RHE) scale using the Nernst equation:

$$E_{RHE} = E_{Ag/AgCl} + 0.197 + 0.059\ pH$$

where 0.197 V is the potential of the Ag/AgCl reference electrode at pH 0. Linear sweep voltammetry (LSV) measurements were performed in 1 M KOH (pH = 14) at a scan rate of 5 mV s^{-1}. The overpotential (η) was calculated from the LSV curves using the equation: $\eta = 0 - E$ (*vs.* RHE). The Tafel slope (b) was determined from the Tafel plot using the equation: $\eta = a + b\log|j|$, where a is the Tafel intercept, j is the current density, and b is the Tafel slope. Cyclic voltammetry (CV) was performed in the potential range of 0.0 to 0.1 V at various scan rates to determine the electrochemical C_{dl}. The C_{dl} was calculated using the following equation: $C_{dl} = (J_a + |J_c|)/2\nu$, where J_a and J_c are the anodic and cathodic current densities, respectively, and ν is the scan rate. The electrochemical surface area (ECSA) was estimated from the C_{dl} values using the equation: ECSA = C_{dl}/C_s, where C_s is the specific capacitance of a planar surface, which was assumed to be 40 μF cm^{-2}, a value commonly adopted in alkaline electrolytes (1 M KOH) as an average reference in the literature.[16,17] Electrochemical impedance spectroscopy (EIS) was performed in the frequency range of 0.1 to 100 000 Hz using an AC amplitude of 10 mV. Measurements were recorded at an overpotential corresponding to a current density of 10 mA cm^{-2}. For consistency across all samples, EIS was conducted at −0.307 V *vs.* RHE, which represents the lowest overpotential required to reach 10 mA cm^{-2}, as determined from the linear LSV curves of the FeCrO-3 catalyst.

Finally, chronopotentiometry was employed to assess the long-term stability of the optimal catalyst for 10 hours.

3. Results and discussion

3.1. Materials characterization

3.1.1. Succinate-based iron and chromium precursors. The FTIR spectra of all precursors are shown in Fig. 2. For Fe(III) succinate (Fe-Succ), the COO^- ions exhibit a strong asymmetric stretching vibration ($\nu_{as}(COO^-)$) at 1580 cm^{-1} and a weak symmetric stretching vibration ($\nu_s(COO^-)$) at 1427 cm^{-1}. In chromium succinate (Cr-Succ), these bands are observed at 1580 cm^{-1} ($\nu_{as}(COO^-)$) and 1401 cm^{-1} ($\nu_s(COO^-)$). The difference between the asymmetric and symmetric stretching frequencies ($\Delta\nu$) provides insights into the coordination mode of the carboxylate group to the metal ion. A larger $\Delta\nu$ value suggests a bidentate coordination mode, where the carboxylate group binds to the metal ion through both oxygen atoms. For Fe-Succ and Cr-Succ, the $\Delta\nu$ values of 153 cm^{-1} and 179 cm^{-1}, respectively, indicate a bidentate coordination of each carboxylate group to the Fe(III) and Cr(III) ions. The Cr-doped Fe-Succ samples exhibit similar IR spectra to the undoped Fe-Succ, suggesting a similar coordination environment for the carboxylate groups. The absence of absorption bands attributable to Cr–O bonds indicates that the Cr^{3+} ions of Cr-Succ are likely incorporated into the Fe-Succ lattice rather than forming separate Cr–O phases. The bands at approximately 1288 cm^{-1} and 1176 cm^{-1} can be assigned to the symmetric and asymmetric stretching vibrations of the C–C bond, respectively.[18] The bands at around 987 cm^{-1} and 674 cm^{-1} are attributed to the O–H bending mode and the H_2O wagging mode, respectively. The vibrations at 550 cm^{-1} and 377 cm^{-1} are assigned to Fe–O vibrations. The IR spectra confirm the successful formation of metal-based succinate precursors with bidentate coordination of the carboxylate groups to the metal ions. The Cr-doped samples show similar coordination environments, suggesting that Cr ions are likely incorporated into the Fe-Succ lattice.

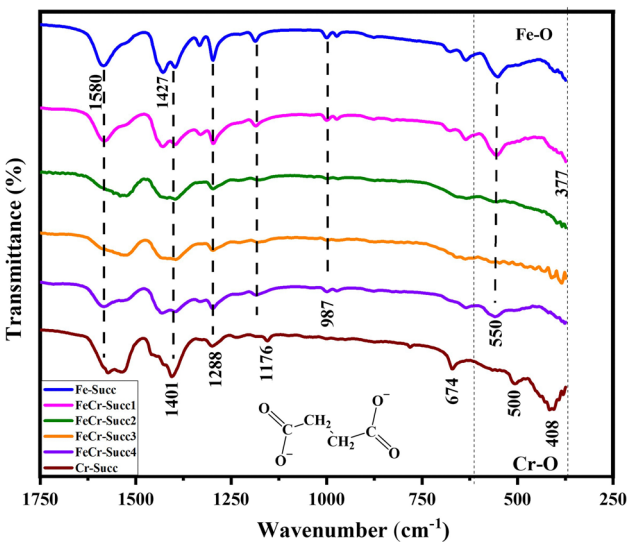

Fig. 2 FTIR spectra of pristine Fe-Succ, Cr-Succ and all the Cr-doped Fe succinates (FeCr-Succ1, FeCr-Succ2, FeCr-Succ3 et FeCr-Succ4).

The UV-vis results of all the precursors are as shown in Fig. S1 (see SI). Fe-Succ exhibits a prominent absorption band in the visible region, centered around 500 nm. This is likely due to ligand-to-metal charge transfer (LMCT) transitions involving the succinate ligand and the Fe^{3+} ion. Cr-Succ shows absorption bands at approximately 420 nm, 579 nm, and possibly a broader one around 709 nm. These bands are likely due to d–d transitions within the Cr^{3+} ion. The spectra of the mixed succinates (FeCr-Suc1, FeCr-Suc2, FeCr-Suc3, FeCr-Suc4) show absorption features that are a combination of those observed for Fe-Succ and Cr-Succ. They exhibit absorption bands in both the UV and visible regions. Bands at 225 and 270 nm are likely due to $\pi \rightarrow \pi^*$ transitions within the succinate ligand. Band at 709 nm could be due to a d–d transition ($^4A_{2g} \rightarrow {}^2T_{1g}$) within the Cr^{3+} ion.[19] This absorption behavior reflects the presence of Cr within the Fe-Succ structure. The UV-Vis spectra of the mixed Fe–Cr succinates indicate that the incorporation of Cr^{3+} into the Fe-Succ structure leads to the formation of new absorption bands in the UV and visible regions. This suggests that the electronic structure of the mixed compounds is different from that of the individual Fe-Succ and Cr-Succ compounds. The presence of Cr^{3+} ions within the Fe-Succ structure likely perturbs the electronic structure of the Fe^{3+} ions and the succinate ligands, as observed by the changes in the absorption spectra. The FTIR spectra confirm the bidentate coordination of succinate to both Fe^{3+} and Cr^{3+} ions, supporting its role in stabilizing the precursor structure. This coordination could be essential for achieving uniform doping and controlled crystallite formation during thermal decomposition.

3.1.2. Residues obtained from thermal decomposition of precursors. Fig. 3a presents the Fourier transform infrared (FTIR) spectra of Fe_2O_3, Cr_2O_3, and Cr-doped Fe_2O_3 samples (FeCrO-1, FeCrO-2, FeCrO-3, and FeCrO-4). The spectra show minimal absorption in the 3000–700 cm^{-1} range, indicating the effective removal of organic components during thermal decomposition. The peaks observed in the FT-IR spectra were assigned to specific bond vibrations and frequencies. For Cr_2O_3 sample, the sharp peaks observed at 602 cm^{-1} were assigned to the ν(O–Cr–O) symmetric bond stretching, indicating the presence of These peaks suggest that the Cr_2O_3 have a crystalline structure, as they indicate the presence of strong chemical bonds. A band appearing at 891 cm^{-1} is characteristic of Cr–O–Cr vibrations. Peaks at 404 cm^{-1} and 497 cm^{-1} are assigned to the Cr–O bond frequency and O vacancies in Cr_2O_3 nanoparticles, respectively. The presence of oxygen vacancies can significantly influence the material's physical and chemical properties.[20] The Fe–O bond is responsible for the vibration bands around 516 cm^{-1} and 427 cm^{-1} in Fe_2O_3. The Cr-doped Fe_2O_3 samples exhibit similar FTIR spectra to Fe_2O_3, with strong absorption bands at 516 cm^{-1} and 427 cm^{-1}. The absence of any absorption bands related to Cr–O in the Cr-doped Fe_2O_3 is a clear indication that the obtained materials are not composite materials but rather doped Fe_2O_3.

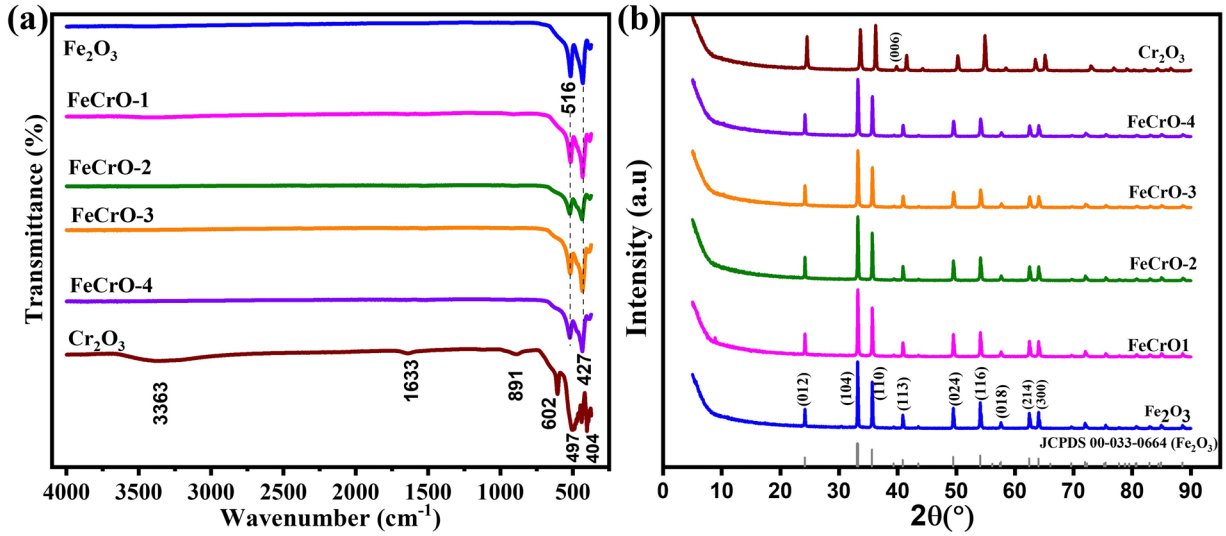

Fig. 3 (a) FTIR spectra; (b) XRD patterns of pristine Fe_2O_3, Cr_2O_3 and all the Cr-doped Fe_2O_3 (FeCrO-1, FeCrO-2, FeCrO-3 and FeCrO-4).

The FTIR spectra confirm the successful synthesis of Cr_2O_3 and Cr-doped Fe_2O_3 nanoparticles. The presence of characteristic vibrational bands indicates the formation of the desired compounds with the expected chemical bonds. The incorporation of Cr into the Fe_2O_3 lattice is evident from the absence of distinct Cr–O bands, suggesting a well-integrated structure.

The structure state and the crystalline nature of the calcined precursors (Fe-Succ, Cr-Succ, FeCr-Suc1, FeCr-Suc2, FeCr-Suc3, and FeCr-Suc4) were investigated using X-ray diffraction (XRD) analysis, as depicted in Fig. 3b. The XRD patterns of both undoped and Cr-doped samples (Fe_2O_3, FeCrO-1, FeCrO-2, FeCrO-3, and FeCrO-4) exhibited diffraction peaks corresponding to the (012), (104), (110), (113), (024), (116), and (300) planes of the hematite (α-Fe_2O_3) phase which peaked at 2θ = 24.2°, 33.1°, 35.6°, 40.9°, 49.5°, 54.1°, and 64°, respectively indexed to the JCPDS standard pattern 01-086-2368 (space group: $R\bar{3}c$ (167), a = 5.036 Å, b = 5.036 Å, c = 13.75 Å). No additional peaks associated with impurity phases, such as metallic iron or magnetite (Fe_3O_4), were detected in any sample. Hence the undoped and Cr-doped samples had the same crystal structure and only the α-Fe_2O_3 phase existed. The average crystalline sizes for all samples were estimated using the Debye–Scherrer formula applied to the (104) peak.

$$D = \frac{0.94 \times \lambda}{\beta \cos\theta}$$

where λ is the wavelength of X-ray used (1.5406 Å), β is the full width at half maximum (FWHM) in radians, and θ is Bragg's diffraction angle.

The average crystallite size decreased from 49.14 nm to 38.19 nm (Table 1) with increasing Cr-doping, as evident from the gradual reduction in the intensity of the (104) XRD peak (Fig. S2a). A noticeable shift in the XRD peak position towards higher angles was observed compared to the reference powder (Fig. S2b). The modification observed could be a consequence of the increasing incorporation of smaller chromium(III) ions (ionic radius: 0.615 Å) in place of the larger iron(III) ions (ionic radius: 0.645 Å) as the chromium content increased (Table 1). This substitution process resulted in a contraction of the α-Fe_2O_3 crystal lattice.[21–23] The ensuing lattice shrinkage within the α-Fe_2O_3 matrix generated increased internal stress and restricted the development of crystallites.[24] This result suggests that Cr-doping affects the crystallite structure of α-Fe_2O_3, as further confirmed by the EDS, electrochemical and optical analyses.

Table 1 Influence of Cr doping on the crystallographic properties of Fe_2O_3

Sample	2θ (°) (104) XRD line	FWHM	Crystallite size [nm]
Fe_2O_3	33.06	0.17606	49.14
FeCrO-1	33.22436	0.1871	46.26
FeCrO-2	33.23066	0.19341	44.75
FeCrO-3	33.24588	0.22663	38.19
FeCrO-4	33.24588	0.22663	38.19
Cr_2O_3	36.2595 (110)	0.22953	38.02

Importantly, the XRD patterns of the chromium-doped samples showed no evidence of segregated chromium phases, especially oxides, initially implying that chromium was integrated into the α-Fe_2O_3 lattice structure.

The morphologies of undoped Fe_2O_3 and Cr-doped Fe_2O_3 oxides were examined using SEM and scanning transmission electron microscopy (STEM), with results presented in Fig. 4 and Fig. S3, respectively. These imaging techniques provide complementary insights into the structural evolution induced by Cr incorporation. The SEM images reveal distinct trends in particle size, shape, and agglomeration as Cr content increases.

All samples form dense micro-scale aggregates, likely resulting from thermal-induced agglomeration during the pyrolysis step. The undoped Fe_2O_3 (Fig. 4a) exhibits a relatively uniform distribution of spherical to slightly elongated particles, with comparatively less agglomeration than the doped samples. As the Cr-doping level increases from FeCrO-1 (Fig. 4b) to

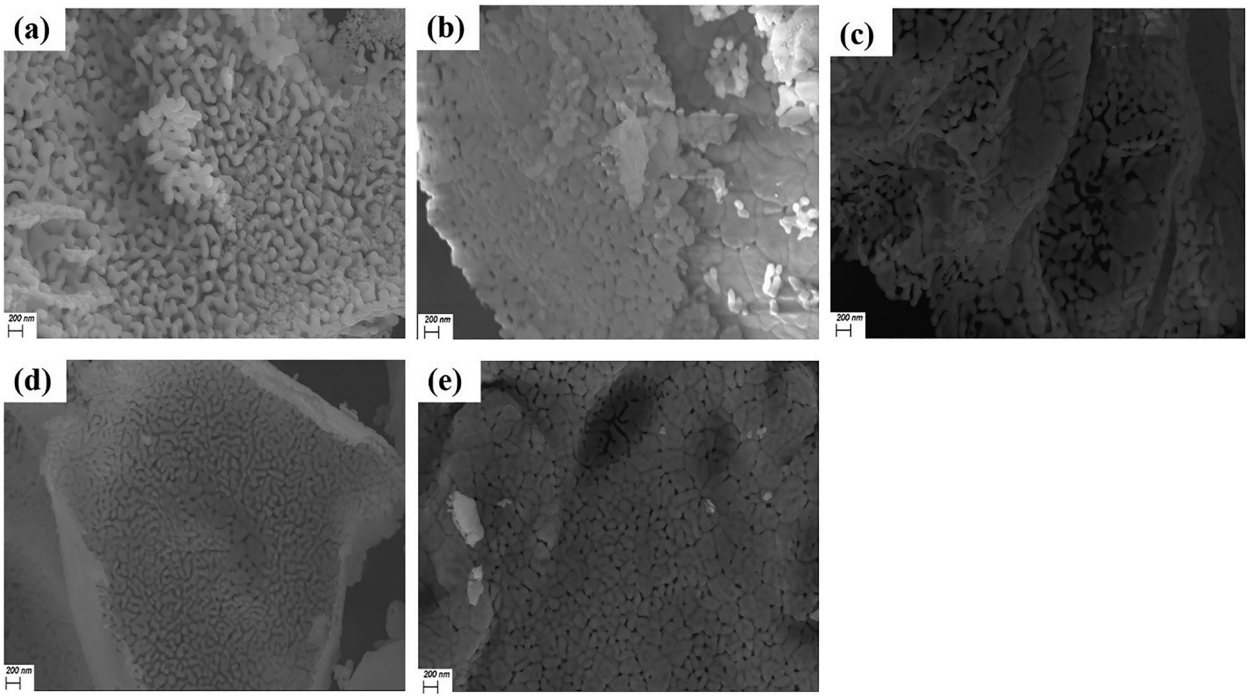

Fig. 4 SEM images of (a) Fe_2O_3 and Cr-doped Fe_2O_3, (b) FeCrO-1 (c) FeCrO-2, (d) FeCrO-3 and (e) FeCrO-4.

FeCrO-4 (Fig. 4e), several morphological changes are observed: a general decrease in average particle size, a transition from spherical to more irregular and angular shapes, and an increase in agglomeration.

These changes suggest that Cr ions disrupt the regular growth of Fe_2O_3 particles and increase surface energy, promoting aggregation to minimize exposed surface area.

STEM imaging, performed on samples prepared from catalyst ink to reflect operational morphology, confirms and refines these observations. Pristine Fe_2O_3 (Fig. S3a) forms dense clusters of relatively large particles (80–90 nm), while Cr-doped samples exhibit finer and more dispersed morphologies. FeCrO-1 and FeCrO-2 (Fig. S3b and c) show moderate size reduction and partial clustering, whereas FeCrO-3 (Fig. S3d) presents the most refined structure, with particles averaging $\sim$ 56 nm and minimal aggregation. FeCrO-4 (Fig. S3e) shows a slight increase in particle size and renewed clustering, suggesting a saturation effect at higher Cr content.

The particle size distribution derived from SEM analysis (Fig. S4) reports average sizes of 82.58 nm (Fe_2O_3), 76.00 nm (FeCrO-1), 69.51 nm (FeCrO-2), 56.07 nm (FeCrO-3), and 76.80 nm (FeCrO-4). These results corroborate the XRD analysis, which predicts a decrease in crystallite size due to lattice distortion induced by Cr doping. In addition to lattice effects, Cr incorporation likely promotes grain boundary formation, contributing to morphological refinement and stabilization of smaller grains. This hypothesis is supported by atomistic simulations showing that Cr atoms tend to segregate at grain boundaries, reducing their mobility and inhibiting grain growth[25] and STEM images (Fig. S3). The resulting defect-rich regions serve as catalytically active sites, enhancing the material's functional performance.[26]

Table 2 Metallic ratio in Cr-doped samples

Sample		FeCrO-1	FeCrO-2	FeCrO-3	FeCrO-4
Atomic percentage (at%)	O	57.7	52.26	48.18	45.11
	Fe	41.59	46.03	49.07	51.41
	Cr	0.71	1.71	2.75	3.48
Atomic metallic ratio (theorical)		0.02	0.040	0.055	0.065
(experimental)		0.017	0.036	0.053	0.060

The elemental mapping analysis presented in Fig. S5 reveals a homogeneous distribution of both Cr and Fe elements within the material. This confirms the successful dispersion of Cr within the Fe_2O_3 matrix. Energy-dispersive X-ray (EDX) spectroscopy was employed to characterize the elemental composition of all Cr-doped Fe_2O_3 samples ($Cr_xFe_{2-x}O_3$). The resulting EDX images, depicted in Fig. S6, unequivocally demonstrate the presence of chromium (Cr), oxygen (O), and iron (Fe) elements. These findings, associated with XRD results, corroborate the successful incorporation of Cr^{3+} into the Fe_2O_3 host lattice and the high purity of the synthesized samples. The estimated and are presented in Table 2. A progressive decrease in the atomic percentage of oxygen was observed with increasing Cr-content in the samples, indicating the presence of oxygen vacancies, as confirmed by the FTIR bands and previous work.[20] Although pyrolysis was conducted under ambient air conditions, the formation of oxygen vacancies could be explained by several factors. First, the substitution of Fe^{3+} by Cr^{3+} introduces local lattice distortion, which lowers the oxygen binding energy and facilitates oxygen release under thermal stress. Second, the elevated temperature during pyrolysis promotes atomic rearrangement and defect mobility, enabling vacancy formation

even in an oxidizing atmosphere.[27] The observed decrease in oxygen content is directly correlated with a concomitant increase of the percentages of iron within the samples as the Cr-concentration is elevated. Nonetheless, the metal ratios remain remarkably close to the theoretical values.

3.2. Optical properties of metal oxides

The UV-visible diffuse reflectance spectra of all metal oxides were recorded, and the results are presented in Fig. 5a. Cr_2O_3 exhibited two absorption bands at 458 nm and 601 nm, attributed to the electronic transitions from ^4A_2g to ^4T_1g and ^4A_2g to ^4T_2g of Cr^{3+} ions in an octahedral coordination environment, consistent with literature reports.[28] The absorption band in the UV region (around 300–350 nm) for Fe_2O_3 is assigned to a ligand-to-metal charge transfer transition from O^{2-} (2p) to Fe^{3+} (3d), while the band in the visible region (around 500–560 nm) is attributed to a double excitation process involving the $^6A_1 \rightarrow {}^6A_1$ and $^6A_1 \rightarrow {}^4T_1$ transitions.[29] A notable enhancement in absorption in the 720–800 nm region was observed for all samples Fe_2O_3 and Cr-doped Fe_2O_3 except Cr_2O_3, which may be associated with oxygen vacancies and particle agglomeration.[30] With increasing Cr doping, a significant increase in absorbance intensity in the visible range was observed. Tauc's relation was employed to evaluate the optical band gap energy (E_g) of all oxides. By extrapolating the linear portion of the $(\alpha h\nu)^2$ *vs.* $h\nu$ plot to the $(\alpha h\nu)^2 = 0$ axis (Fig. S7), the band gap values were estimated. A systematic decrease in E_g was observed with increasing Cr-doping, correlating with the gradual color change from the earth red of Fe_2O_3 to the dark brown of FeCrO-4 (Fig. S8). The band gap decreased from 1.94 eV for Fe_2O_3 (consistent with literature values[31]) to 1.92 eV, 1.73 eV, 1.69 eV, and 1.48 eV for FeCrO-1, FeCrO-2, FeCrO-3, and FeCrO-4, respectively (Fig. 5b). This red shift in the band gap can be attributed to the introduction of defect states or crystallite size effects. The incorporation of Cr ions into the Fe_2O_3 lattice can create additional energy levels within the band gap, acting as defect states. These defect states facilitate electronic transitions with lower energy requirements, leading to a reduced band gap. When a photon is absorbed, electron–hole pairs are generated, and the presence of these defect states lowers the energy barrier for the transition of electrons from the valence band to the conduction band compared to undoped Fe_2O_3. Furthermore, the observed decrease in oxygen content, as evidenced by EDX and FTIR analyses, could also contribute to the reduction in the band gap. Oxygen vacancies can act as electron donors, creating localized states within the band gap and facilitating electronic transitions with lower energy requirements.

3.3. Electrocatalytic performance of metal oxides

Linear sweep voltammetry analyses were undertaken on all metal oxide samples in a 1 M KOH electrolyte utilizing a tri-electrode configuration. For the purpose of comparison, the performance of the synthesized materials was appraised against GC and Pt/C-20%, with the findings illustrated in Fig. 6.

The LSV curves, as illustrated in Fig. 6a, exhibit a reduction in overpotential at a current density of 10 mA cm^{-2} (η_{10}) as the degree of Cr doping within the Fe_2O_3 increases.

Fig. 6b reveals that the η_{10} values for the chromium-doped Fe_2O_3 samples are notably lower than those for pristine Cr_2O_3 and Fe_2O_3, with specific values of 371, 332, 307, and 326 mV recorded for FeCrO-1, FeCrO-2, FeCrO-3, and FeCrO-4, respectively. These are contrasted against a value of 433 mV for undoped Fe_2O_3 and an almost negligible HER activity for Cr_2O_3. This suggests that the Cr-doped Fe_2O_3 samples exhibit superior HER activity, with FeCrO-3 showing the lowest overpotential among the doped variants, likely due to an optimal integration of chromium into the Fe_2O_3 lattice. Further, SEM and XRD analyses indicated that FeCrO-3 consists of nanoparticles possessing a reduced size in comparison to other doped samples, as detailed in Table 2. This characteristic affords an enlarged surface area for electrocatalytic activities, thereby enhancing the HER performance. That could explain why FeCrO-4 (76.8 nm showed by SEM) has higher potential than FeCrO-3 (56.07 nm showed by SEM)[32] Previous scholarly works have documented η_{10} values of 536 mV for Fe_2O_3 synthesized *via* the thermal decomposition of iron(III) malonate.[33] The observed differences might be attributed to the choice of ionic

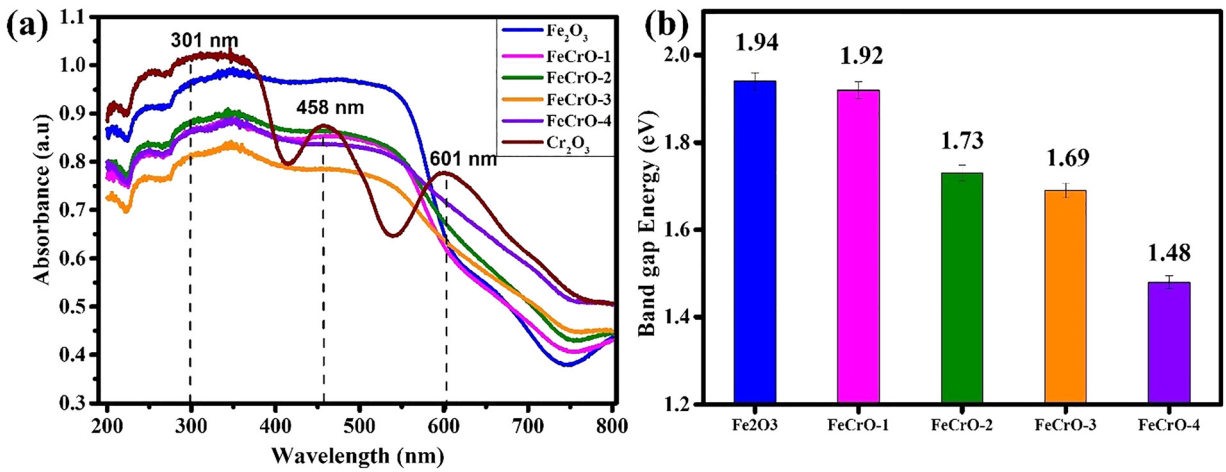

Fig. 5 (a) UV-visible spectra, and (b) energy bandgap of Fe_2O_3, Cr_2O_3 and all the Cr-doped Fe_2O_3 (FeCrO-1, FeCrO-2, FeCrO-3 and FeCrO-4).

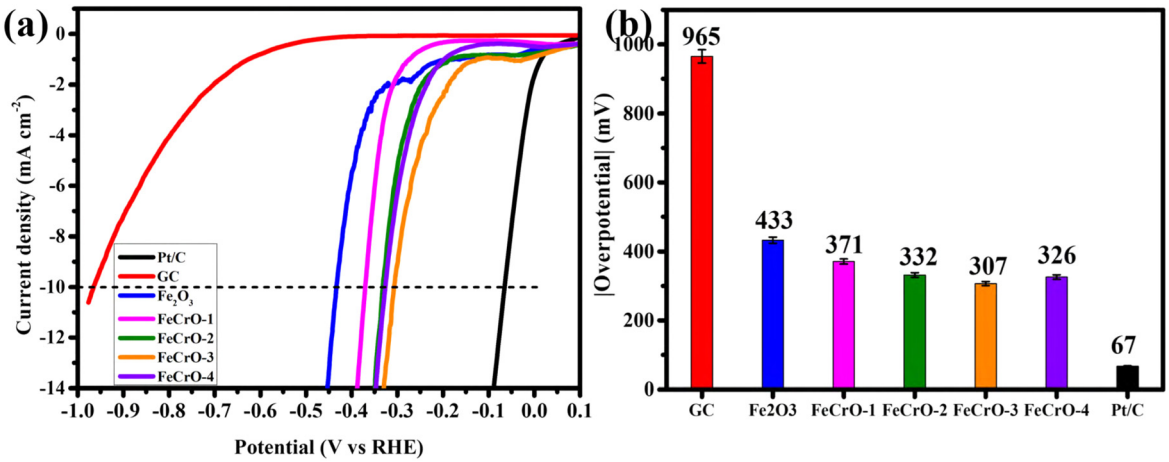

Fig. 6 Electrochemical performance for HER in alkaline medium (1 M KOH): (a) linear sweep voltammetry (LSV) curves at 10 mV s^{-1} for Pt/C, GC, Fe_2O_3, and Cr-doped Fe_2O_3 samples. (b) Overpotential values at 10 mA cm^{-2} for the same materials. Error bars represent standard deviation from triplicate measurements.

ligands used during synthesis. To elucidate the influence of chromium doping on the kinetics of the HER further, Tafel slopes were generated to explore the correlation between overpotential and current density, as depicted in Fig. 7a. The Tafel slope (TS) was determined to be 135 mV dec^{-1} for Fe_2O_3, aligning with established literature.[33] Conversely, the Cr-doped variants displayed TS values of 84, 118, 130, and 168 mV dec^{-1} for FeCrO-1, FeCrO-2, FeCrO-4, and FeCrO-3, respectively (Fig. S9).

It is generally desirable for an electrocatalyst to exhibit the lowest possible Tafel slope. The findings suggest that Fe_2O_3 doped with lower chromium levels (2 at% and 4 at%) significantly reduces the Tafel slope relative to pure Fe_2O_3. In particular, FeCrO-1, with a Tafel slope of 84 mV dec^{-1}, exhibits improved kinetics for the hydrogen evolution reaction (HER). This implies that minimal Cr doping enhances charge transfer efficiency and boosts HER kinetics. A diminished Tafel slope typically indicates a catalyst's higher efficiency, signifying a quicker reaction rate.

The HER is a two-step electron transfer reaction that occurs at the catalyst surface, proceeding *via* the Volmer–Heyrovsky or Volmer–Tafel mechanisms. The HER in an alkaline medium involves the following steps:[34]

Volmer–Heyrovsky mechanism:

Water dissociation: $H_2O + * + e^- \rightarrow H^* + OH^-$ (Volmer step)

Hydrogen desorption: $H^* + H_2O + e^- \rightarrow H_2 + OH^-$ (Heyrovsky step)

Volmer–Tafel mechanism:

Water dissociation: $H_2O + * + e^- \rightarrow H^* + OH^-$ (Volmer step)

Hydrogen recombination: $2H^* \rightarrow H_2$ (Tafel step)

(* denotes an active site on the catalyst).

According to established HER kinetics, Tafel slopes of approximately 120, 40, and 30 mV dec^{-1} are typically associated with Volmer, Heyrovsky, and Tafel rate-limiting steps, respectively.[35] In this study, the TS values obtained for Fe_2O_3

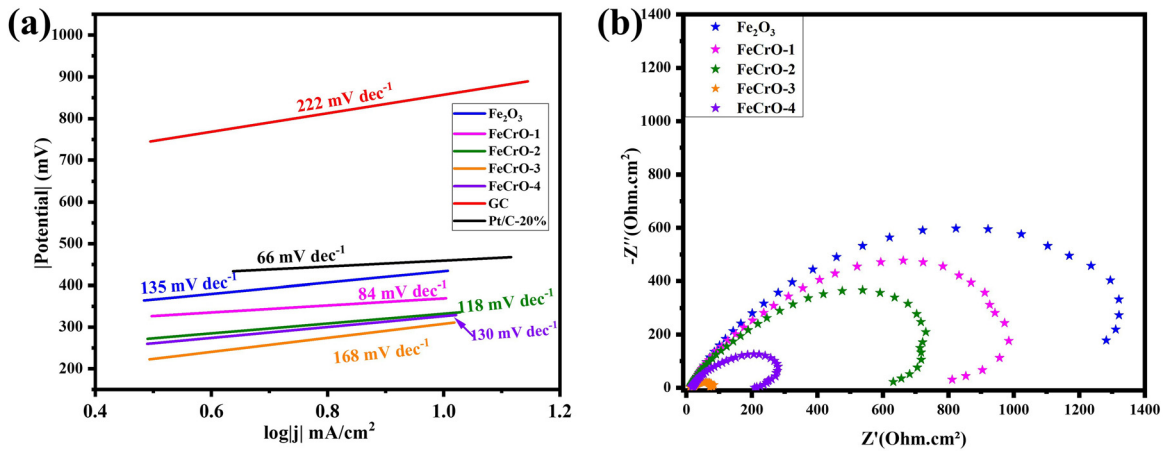

Fig. 7 (a) Tafel plots and (b) EIS Nyquist plots for Fe_2O_3, and Cr-doped Fe_2O_3 samples.

and Cr-doped Fe_2O_3 samples ranged from 84 to 156 mV dec^{-1}. These values initially suggested that the HER mechanism was likely governed by the Volmer step, involving the adsorption of hydrogen intermediates (H*) onto the catalyst surface. This interpretation was subsequently reinforced by the EIS and distribution of relaxation times (DRT) analyses, which revealed slow interfacial charge transfer and adsorption-related processes. Together, these results confirmed that the initial electron transfer remains the rate-limiting step in the HER pathway for these materials.

To delve deeper into the electrode–electrolyte interface kinetics during HER, EIS was performed at the overpotential necessary to achieve a current density of 10 mA cm^{-2} in 1 M KOH (−0.307 V *vs.* RHE), as shown in Fig. 7b. The Nyquist plots of all Cr-doped Fe_2O_3 samples exhibit a single depressed semicircle, characteristic of charge transfer resistance (R_{ct}) associated with HER kinetics.[36] Compared to pristine Fe_2O_3. ($R_{ct} \approx 1300\ \Omega$), Cr-doped samples show significantly reduced R_{ct} values: approximately 280 Ω for FeCrO-1, 790 Ω for FeCrO-2, 990 Ω for FeCrO-4, and notably 50 Ω for FeCrO-3. This confirms that Cr doping enhances interfacial charge transfer, with FeCrO-3 exhibiting the most efficient electron transport among the studied compositions.

The improved EIS performance of FeCrO-3 is attributed to multiple synergistic factors. First, its smaller particle size increases the electrochemically active surface area (ECSA), thereby exposing a greater number of accessible catalytic sites. This morphological refinement facilitates more efficient charge transfer at the electrode/electrolyte interface. Second, Cr-induced lattice distortions and defect formation enhance conductivity by promoting electron mobility across the oxide matrix.

The EIS spectra reveal contributions from solution resistance, charge transfer resistance, and interfacial capacitive effects. While no classical Warburg-type diffusion tail is observed under the present experimental conditions,[37,38] a slight inductive response emerges at low frequencies in some samples, particularly FeCrO-1, FeCrO-2 and FeCrO-4. This feature is not a true inductive loop but rather a manifestation of interfacial relaxation phenomena such as intermediate adsorption or surface restructuring of the Fe–Cr oxide layer. Similar low-frequency responses have been reported for HER and OER catalysts in alkaline media.[39]

To resolve overlapping electrochemical processes that may be obscured in Nyquist plots, a DRT analysis was performed (Fig. S10). By translating the impedance response into a spectrum of relaxation time constants, this approach isolates individual electrochemical processes without relying on any assumed circuit layout.[40] In general, all Cr-doped Fe_2O_3 samples exhibit multiple relaxation features, typically with one peak in the high-frequency region ($\log\tau \approx -2$ to -3) corresponding to fast charge transfer, and another in the lower-frequency domain ($\log\tau \approx 0$ to 1) associated with slower interfacial phenomena.[40] Among them, FeCrO-3 stands out with the most clearly resolved and intense dual-peak profile. It displays a sharp, narrow peak at $\log\tau \approx -2.5$, indicative of rapid electron transfer, and a well-defined secondary peak at $\log\tau \approx 0.5$, reflecting slower surface dynamics. This distinct separation of relaxation times aligns with its exceptionally low R_{ct} and supports its superior HER performance. In contrast, other Cr-doped samples show broader and less resolved DRT profiles, suggesting more complex and less efficient interfacial behavior. The conductivity of the Cr-doped Fe_2O_3 electrocatalysts was further evaluated through EIS. As Cr content increased, the R_{ct} decreased significantly, indicating enhanced electron mobility within the catalyst matrix. This improvement in conductivity is consistent with previous studies on doped transition metal oxides, where lattice distortion and defect engineering contribute to better charge transport.[41,42] These findings reinforce the role of Cr doping not only in modifying the electronic structure but also in facilitating efficient charge transfer during the HER process.

Cyclic voltammetry (CV) was employed to further evaluate the electrocatalytic performance of various materials through the analysis of double-layer capacitance (C_{dl}) (Fig. S11). This was achieved by conducting CV measurements at varying scan rates ranging from 10 to 100 mV s^{-1} within the non-faradaic region (0.0–0.1 V). Subsequently, the corresponding electrochemically active surface area (ECSA) was calculated. Fig. 8 illustrates the linear relationship between the current density difference and scan rate at a potential of 0.05 V in a 1 M KOH solution. The C_{dl} (and the associated ECSA) values for Fe_2O_3, Cr_2O_3, FeCrO-1, FeCrO-2, FeCrO-3, and FeCrO-4 were determined to be 444 μF cm^{-2} (11.1), 52.27 μF cm^{-2} (1.3), 5140 μF cm^{-2} (128.5), 3330 μF cm^{-2} (83.2), 3330 μF cm^{-2} (83.2), and 1090 μF cm^{-2} (27.2), respectively.

The observed increase in double-layer capacitance (C_{dl}) from 444 μF cm^{-2} for pure Fe_2O_3 to 5140 μF cm^{-2} for FeCrO-1 upon Cr-doping signifies a substantial enhancement in the number of active sites available for electrochemical reactions. Notably, FeCrO-1 exhibits the highest electrochemically active surface area (ECSA) among all samples. The maximal ECSA and C_{dl} values observed for FeCrO-1 could likely be attributed to a potentially optimal effect of the low Cr-doping level (2 at%),

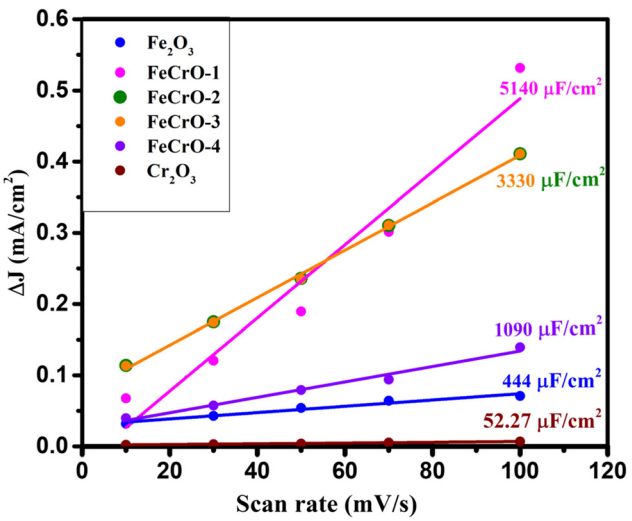

Fig. 8 Scan rate dependence of the current densities at 0.05 V of pristine Fe_2O_3, Cr_2O_3 and all the Cr-doped Fe_2O_3 (FeCrO-1, FeCrO-2, FeCrO-3 and FeCrO-4.

which might have engendered a significant number of active sites and favorably modified the surface morphology (with lowest particle's agglomeration). This is likely due to the formation of defects within the Fe_2O_3 lattice when Fe^{3+} ions are substituted by a smaller Cr^{3+} ions. These defects (oxygen vacancies) serve as new active sites, thereby increasing the overall surface area available for electrochemical processes.

However, when the amount of Cr-doping exceeds that doping level, as observed in FeCrO-2, FeCrO-3, and FeCrO-4, the particles tend to agglomerate, leading to a reduction in the effective surface area for reactions. This agglomeration is evident from the SEM images and results in a decrease in the number of accessible active sites. Consequently, while there is an initial increase in C_{dl} with Cr-doping, excessive Cr leads to lower C_{dl} values due to the reduced availability of active sites resulting from increased particle clustering.

FeCrO-1, which exhibits the lowest Tafel slope (84 mV dec^{-1}) and highest ECSA (128.5), might intuitively be expected to deliver the lowest overpotential. However, this was not observed. A plausible explanation lies in the trade-off between intrinsic site activity, particle morphology, and charge transport dynamics. FeCrO-1, with its lower Cr content and larger particle size (76 nm), possesses highly active sites (C_{dl} = 5140 μF cm^{-2}) but suffers from limited specific surface area and potentially less efficient charge mobility. In contrast, FeCrO-3, despite having a lower ECSA as indicated by its smaller C_{dl} (3330 μF cm^{-2}) demonstrates superior catalytic performance. This enhancement is attributed to its smaller particle size (56.07 nm), which increases the number of exposed sites, and more importantly, its significantly lower R_{ct}, reflecting improved electron transfer kinetics. The enhanced conductivity of FeCrO-3 likely stems from Cr-induced lattice distortions and defect formation, which facilitate charge mobility across the electrode–electrolyte interface. Additionally, the spatial distribution of catalyst particles within the Nafion matrix may favor better connectivity and ionic accessibility in FeCrO-3, compensating for its lower ECSA. These synergistic effects collectively contribute to its reduced overpotential and steeper Tafel slope, underscoring the importance of conductivity and interfacial architecture in governing HER performance.

In summary, the data suggest that Cr-doping improves the electrochemical performance of Fe_2O_3 by increasing the number of active sites up to an optimal level.

The long-term stability of FeCrO-3, which exhibited the lowest overpotential among all Cr-doped Fe_2O_3 samples, was assessed using chronopotentiometry. The stability test was conducted for 15 hours at a fixed current density of 10 mA cm^{-2}, with the results depicted in Fig. 9a. The overpotential remained essentially constant throughout the test, exhibiting a minimal increase of only 15 mV, indicative of excellent electrochemical stability during sustained operation. This behavior could be attributed to the robust integration of Cr^{3+} into the Fe_2O_3 lattice, which enhances defect formation and stabilizes the catalytic surface. The overpotential drift of only 15 mV over 15 h is notably modest. For instance, the electrodeposited $CoFe_2O_4$ catalyst reported by Zhang *et al.* maintained stable activity for several hours of alkaline HER operation, confirming that such low degradation rates are characteristic of robust oxide catalysts.[43] To further corroborate the stability of FeCrO-3, a continuous LSV was performed subsequent to the chronopotentiometry test. Post-stability LSV measurements (Fig. 9b) revealed only a minor shift in overpotential at 10 mA cm^{-2} confirming that the catalyst retained its HER activity without signs of significant degradation. These results demonstrate that FeCrO-3 possesses both high catalytic activity and structural stability, making it a promising candidate for long-term alkaline water electrolysis.

Compared to other nanoelectrocatalysts reported in recent literature,[44,45] our Cr-doped Fe_2O_3 system exhibits competitive overpotential values and stability, while benefiting from a simple and scalable synthesis route.

Table 3 presents a selection of iron oxide-based materials reported as electrocatalysts for the HER in alkaline media. Notably, the FeCrO-3 electrocatalyst synthesized *via* the straightforward method outlined in this work demonstrates

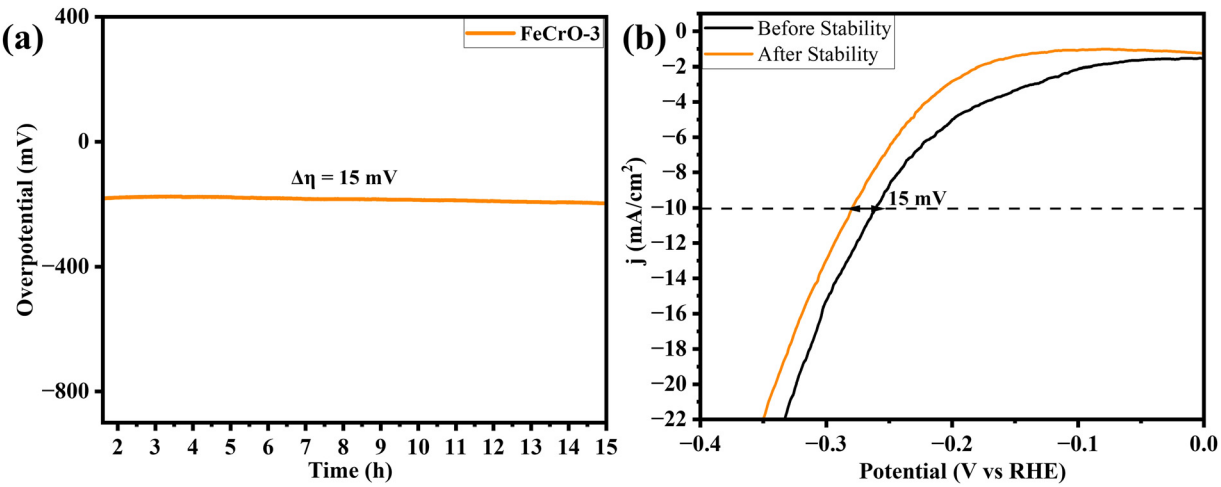

Fig. 9 (a) Chronopotentiometry of the best Cr-doped Fe_2O_3 (FeCrO-3), and (b) its LSV polarization curves before and after chronopotentiometry.

Table 3 Comparison of the electrocatalytic activity of all the prepared materials with other previously reported for HER in 1M KOH

Catalyst	η_{10} [mV]	Tafel slope [mV dec^{-1}]	Scan rate [mV s^{-1}]	Ref.
Niferrite	600	138.9	5	46
$Co_{0.1}Ni_{0.9}$ferrite	566	141.1	5	46
Fe_2O_3	536	142	5	33
$ZnFe_2O_4$	520	144	5	47
Coferrite	422	116.6	5	46
$NiFe_2O_4$	420	133	5	47
Fe_2O_3	**433**	**145**	**5**	**This work**
FeCrO-1	**371**	**128**		
FeCrO-2	**332**	**143**		
FeCrO-4	**326**	**144**		
FeCrO-3	**307**	**164**		

promising characteristics, notably its low overpotential compared to other similar materials and its ability to enhance performance over time. This method, suitable for large-scale production, facilitates molecular-level doping of Fe_2O_3 with Cr, enhancing the material's dispersibility and catalytic activity.

4. Conclusions

In this study, Cr-doped Fe_2O_3 nanomaterials were successfully synthesized *via* a straightforward coprecipitation route using succinate-based precursors. Progressive Cr incorporation (2–6.5 at%) induced a marked bandgap narrowing from 1.92 eV to 1.48 eV, as revealed by optical analysis, indicating beneficial electronic structure modulation. Electrocatalytic tests demonstrated substantial enhancement of HER activity upon doping, with FeCrO-3 (5.5 at% Cr) delivering the best performance an overpotential of 307 mV at 10 mA cm^{-2} surpassing both undoped Fe_2O_3 and other doping levels. STEM/SEM imaging, EIS, and DRT analyses linked this activity to the combined effects of particle size refinement, Cr-induced defect engineering, and markedly reduced charge-transfer resistance, which together enable rapid electron transport and controlled intermediate adsorption. Overall, this work demonstrates that optimal HER performance in Cr-doped Fe_2O_3 arises from the interplay of electronic tuning, defect engineering, particle size refinement, and charge-transfer dynamics rather than from active-site density alone. Beyond HER, the reduced bandgap (1.48 eV) suggests strong potential for photoelectrochemical applications such as the OER in alkaline media under solar illumination. Future studies will employ TEM to probe lattice distortion in greater detail, EPR to quantify oxygen vacancy concentrations, and photoelectrochemical testing to evaluate dual HER/OER capability for overall water splitting. These findings provide valuable design guidelines for high-performance, earth-abundant electrocatalysts for sustainable hydrogen production.

Author contributions

P. K. Y.: data curation, formal analysis, writing – original draft. C. M. K. M.: methodology, investigation (electrochemical performance measurements). B. T.: investigation (SEM analysis), writing – review & editing. B. S.: investigation (SEM analysis), writing – review & editing. K. M.: writing – review & editing. C. Y. N.: writing – review & editing. P. K. T.: writing – review & editing. R. L. F.: supervision, writing – review & editing. All authors have read and approved the final manuscript.

Conflicts of interest

The authors declare no competing financial interest

Data availability

The data supporting this article has been included as part of the supplementary information (SI). Supporting information: UV-visible spectra of all the precursors, additional results including photographs, elemental mapping, STEM images, Tafel plot derived from LSV curves, DRT analysis, Bode plot, EDX spectra, Tauc Plots and particle size distribution of all the Cr-doped Fe_2O_3 samples (PDF). See DOI: **https://doi.org/10.1039/d5ma00634a**.

Acknowledgements

R. L. F. was supported by DAAD Material Resources Programme for Institutions of Higher Education in Developing Countries, by the RSC Research Fund grant no. R23-1928872283 for electrochemical facilities and by DLR-DAAD Senior Scientist Programme.

References

1 J. Wang and W. Azam, *Geosci. Front.*, 2024, **15**, 101757.
2 J. L. Veronica, M. Sofianos, D. S. Silvester, P. K. Samanta, M. Paskevicius, N. J. English and C. E. Buckley, *J. Energy Chem.*, 2020, **56**, 162–170.
3 S. Sun, Z. Wang, S. Meng, R. Yu, D. Jiang and M. Chen, *Nanotechnology*, 2022, **33**, 075204.
4 Y. Jiao, Y. Zheng, M. Jaroniec and S. Z. Qiao, *Chem. Soc. Rev.*, 2015, **44**, 2060–2086.
5 C. Li and J.-B. Baek, *ACS Omega*, 2020, **5**, 31–40.
6 P. Garg, L. Mohapatra, A. K. Poonia, A. K. Kushwaha, K. N. V. D. Adarsh and U. Deshpande, *ACS Omega*, 2023, **8**, 38607–38618.
7 W. L. Kwong, C. C. Lee, A. Shchukarev, E. Björn and J. Messinger, *J. Catal.*, 2018, **365**, 29–35.
8 N. Maley, P. Patel, F. M. de Souza, A. Kumar and R. K. Gupta, *Energy Storage*, 2024, **6**, e70062.
9 X. Lincheng, W. Yue, Y. Yong, H. Zhanzhong, C. Xin and L. Fan, *Appl. Energy*, 2023, **339**, 120931.
10 M. Aalim, I. Irshad, A. M. Tantray, A. Sohail, B. Want and M. A. Shah, *J. Mater. Sci.: Mater. Electron.*, 2023, **34**, 1409.
11 S. Kocabas, A. Cetin, A. Önal and E. Nalbant, *J. Nanopart. Res.*, 2019, **21**, 143.

12 H. Kitaura, K. Takahashi, F. Mizuno, A. Hayashi, K. Tadanaga and M. Tatsumisago, *J. Power Sources*, 2008, **183**, 418–421.
13 J. Zhao, X. Liu, X. Ren, B. Du, X. Kuang, D. Tian, Q. Wei and D. Wu, *J. Colloid Interface Sci.*, 2022, **609**, 414–422.
14 J. S. Borcezi, K. Ramos, A. K. de Oliveira Ouba, A. A. S. Chinelatto, E. C. Grzebielucka, F. C. Monteiro, J. F. H. L. Monteiro, L. P. Wendler and A. L. Chinelatto, *J. Electroceram.*, 2023, **51**, 281–291.
15 L. Luo, X. Zhou, Y. Chen, F. Sun, L. Wang and Q. Tang, *Chem. Sci.*, 2025, **16**, 3598–3610.
16 P. Connor, J. Schuch, B. Kaiser and W. Jaegermann, *Z. Phys. Chem.*, 2020, **234**, 979–994.
17 C. C. L. McCrory, S. Jung, J. C. Peters and T. F. Jaramillo, *J. Am. Chem. Soc.*, 2013, **135**, 16977–16987.
18 R. Lontio Fomekong, P. Yontchoum, T. J. Matemb Ma Ntep, H. Kamta, P. Kenfack Tsobnang, S. Krüger, J. Sturala, Z. Sofer, B. Saruhan, A. Delcorte and J. Lambi, *Adv. Energy Sustainability Res.*, 2023, **5**, 2300232.
19 P. T. Kenfack, E. Wenger, S. Dahaoui, J. N. Lambi, P. Durand, S. Ponou and C. Lecomte, *Acta Crystallogr. Sect. A*, 2014, **70**, C1474.
20 I. Irshad, A. G. Lone and B. Want, *J. Alloys Compd.*, 2024, **971**, 172696.
21 N. Popov, S. Krehula, M. Ristić, E. Kuzmann, Z. Homonnay, M. Bošković, D. Stanković, S. Kubuki and S. Musić, *J. Phys. Chem. Solids*, 2021, **148**, 109699.
22 S. Riaz, A. Akbar and S. Naseem, *IEEE Trans. Magn.*, 2014, **50**, 1–4.
23 H. Liu, S.-H. Luo, D.-X. Zhang, D.-B. Hu, T.-F. Yi, Z.-Y. Wang, Y.-H. Zhang, Y.-G. Liu, Q. Wang, A.-M. Hao, X.-W. Liu and R. Guo, *ChemElectroChem*, 2019, **6**, 856–864.
24 F. Bouhjar, L. Derbali, B. Marí and B. Bessaïs, *Int. J. Hydrogen Energy*, 2020, **45**, 11492–11501.
25 P. Huang, Q. Xiao, W. Hu, B. Huang and D. Yuan, *Metals*, 2024, **14**, 454.
26 D. N. Siddiqui, N. Mehboob, A. Zaman, A. M. Alsuhaibani, A. Algahtani, V. Tirth, S. Alharthi, N. H. Al-Shaalan and M. A. Amin, *ACS Omega*, 2023, **8**, 19892–19899.
27 Y. Wang, Y. Han, W. Suo, J. Zhang, X. Lai, Z. Li, Z. Liang and G. Cao, *Sci. Chin. Mater.*, 2023, **66**, 4357–4366.
28 B. B. Kamble, M. Naikwade, K. M. Garadkar, R. B. Mane, K. K. K. Sharma, B. D. Ajalkar and S. N. Tayade, *J. Mater. Sci.: Mater. Electron.*, 2019, **30**, 13984–13993.
29 K. Arora, H. Kaur, M. Kainth, S. Meena and T. Singh, *RSC Adv.*, 2019, 9.
30 J.-C. Wang, J. Ren, H.-C. Yao, L. Zhang, J.-S. Wang, S.-Q. Zang, L.-F. Han and Z.-J. Li, *J. Hazard. Mater.*, 2016, **311**, 11–19.
31 M. M. Ba-Abbad, A. A. H. Kadhum, A. B. Mohamad, M. S. Takriff and K. Sopian, *Chemosphere*, 2013, **91**, 1604–1611.
32 M. Baumung, F. Schönewald, T. Erichsen, C. A. Volkert and M. Risch, *Sustainable Energy Fuels*, 2019, **3**, 2218–2226.
33 L. O. Matchim Fondjo, R. Lontio Fomekong, P. Kenfack Tsobnang, H. M. Teudjieukeng Kamta, C. Ngnintedem Yonti, P. Mountapmbeme Kouotou and J. Lambi Ngolui, *J. Alloys Compd.*, 2025, **1010**, 176979.
34 N. Mahmood, Y. Yao, J. W. Zhang, L. Pan, X. Zhang and J. J. Zou, *Adv. Sci.*, 2018, **5**, 1700464.
35 R. Lontio Fomekong, S. Akir, F. M. Oliveira, J. Luxa, L. Chacko, J. Regner, L. Dekanovsky, E. Vejmelkova and Z. Sofer, *J. Power Sources*, 2024, **602**, 234293.
36 B.-A. Mei, J. Lau, T. Lin, S. H. Tolbert, B. S. Dunn and L. Pilon, *J. Phys. Chem. C*, 2018, **122**, 24499–24511.
37 J. R. Macdonald, W. B. Johnson, I. D. Raistrick, D. R. Franceschetti, N. Wagner, M. McKubre, D. Macdonald, B. Sayers, N. Bonanos, B. C. H. Steele, E. P. Butler, W. L. Worell, M. Strømme, S. Malmgren, S. Sundaram, G. R. Engelhardt, Y. Barsukov, W. G. Pell, C. M. Roland and R. Eisenberg, *Impedance Spectroscopy: Theory, Experiment, and Applications*, 3rd edn, 2018.
38 A. Lasia and A. Lasia, *Electrochemical Impedance Spectroscopy and its Applications*, Springer, 2014.
39 Z. Qiu, Y. Ma, G. A. Niklasson and T. Edvinsson, *Physchem*, 2021, **1**, 69–81.
40 Z. Wang, *Nat. Rev. Clean Technol.*, 2025, **1**, 453.
41 Q. Ma, J. Sha, B. Chen, E. Liu, C. Shi, L. Ma, F. He, C. He, N. Zhao and J. Kang, *J. Mater. Chem. A*, 2025, **13**, 22009–22019.
42 T. Divya, R. Sarankumar, K. S. Balamurugan, P. Sakthivel and A. Sivakami, *J. Nanopart. Res.*, 2025, **27**, 55.
43 C. Zhang, S. Bhoyate, C. Zhao, P. K. Kahol, N. Kostoglou, C. Mitterer, S. J. Hinder, M. A. Baker, G. Constantinides, K. Polychronopoulou, C. Rebholz and R. K. Gupta, *Catalysts*, 2019, **9**, 176.
44 L. Zhao, M. Wen, Y. Guo, Q. Wu, Q. Zhu and Y. Fu, *Adv. Funct. Mater.*, 2023, **33**, 2308422.
45 J. Yang, X. Liu, J. Liu, Y. Qiu, X. Zhang and L. Zhang, *J. Electroanal. Chem.*, 2022, **918**, 116439.
46 S. Chamani, M. Khatamian, N. S. Peighambardoust and U. Aydemir, *ACS Omega*, 2021, **6**, 33024–33032.
47 H. Belhadj, Y. Messaoudi, M. R. Khelladi and A. Azizi, *Int. J. Hydrogen Energy*, 2022, **47**, 20129–20137.